inventions

Article

Fast Adaptive Beamforming for McWiLL "Korona" Ring Antennas Using Random Forest–Based MVDR

Bogdan M. Khalmatov and Denis S. Chirov *

Department of Radio Engineering Systems, Moscow Technical University of Communications and Informatics, 8A Aviamotornaya St., Moscow 111024, Russia; wotblitzdrd@gmail.com

* Correspondence: d.s.chirov@mtuci.ru

Abstract

This study focuses on accelerating adaptive beamforming in the Multicarrier Wireless Internet Local Loop (McWiLL) professional radio communication system using "Korona" ring smart antennas. The work investigates algorithms for calculating complex weight coefficients in an eight-element uniform circular antenna array. The main objective is to reduce beam pattern adaptation time while maintaining interference suppression depth and robustness under multipath propagation. To achieve this, an ensemble machine learning approach based on the Random Forest algorithm is employed to approximate the optimal Minimum Variance Distortionless Response (MVDR) solution using elements of the sample covariance matrix of received signals. The training dataset is generated through McWiLL channel simulations considering mutual coupling between array elements, signal-to-noise ratio (SNR) variation, and different angles of arrival of the desired and interfering signals. The proposed method is evaluated against the classical MVDR algorithm in terms of radiation pattern null depth, robustness to phase distortions, and inference time on a Field-Programmable Gate Array (FPGA) hardware platform. Results demonstrate that the Random Forest-based approach achieves more than a fourfold reduction in computation time while forming radiation-pattern nulls of about 30–35 dB toward the interferers (versus 44–46 dB for the classical MVDR); the synthesized core uses no hardware multipliers (DSP48), and its functional equivalence to the software model is confirmed by bit-exact RTL co-simulation. The findings show promise for deployment in McWiLL base stations and other professional radio systems requiring fast, adaptive beamforming under dynamic channel conditions.

Keywords: adaptive beamforming; antenna radiation pattern; circular antenna array; communication systems; interference suppression; machine learning; McWiLL; MVDR; random forest; simulation

Academic Editor: Timofey Shevgunov

Received: 27 July 2026
Accepted: 25 August 2026
Published: 27 August 2026

1. Introduction

The current stage of development of telecommunication systems is characterized by an explosive growth in transmitted traffic volumes and increasingly stringent requirements for network spectral efficiency [1]. Under conditions of limited frequency resources, especially in bands below 6 GHz, a key direction in the evolution of professional mobile radio (PMR) systems and fifth-generation (5G) networks is spatial division multiple access (SDMA). The technological basis for implementing this approach is provided by smart antenna systems, which are capable of dynamically adjusting their radiation patterns in response to the signal environment [2–4].

These technologies play a particularly important role in broadband wireless access systems based on the McWiLL standard, which is widely used for building mission-critical communication networks, as well as technological communication systems in transport and the energy sector [5]. A distinctive feature of the McWiLL physical layer, based on Code-spread Orthogonal Frequency Division Multiple Access (CS-OFDMA) technology, is the use of eight-element circular antenna arrays of the "Korona" type. This configuration enables the formation of narrow beams over a full 360-degree sector without the need for multiple sectorized antenna panels, providing a significant gain in link budget and effective suppression of co-channel interference.

The performance of the "Korona" smart antenna directly depends on the speed and accuracy of digital signal processing (DSP) algorithms that compute the weighting coefficients for each antenna element [6]. Classical adaptive methods, such as MVDR [7] and the Multiple Signal Classification (MUSIC) [8] algorithm, ensure high accuracy in placing radiation pattern nulls toward interference sources [9,10]. However, their implementation requires computationally intensive operations, primarily the inversion of large-dimensional covariance matrices.

Under conditions of high user mobility—for example, communication with high-speed trains or emergency service vehicles—the parameters of the radio channel vary faster than classical iterative algorithms (such as LMS—Least Mean Squares) and can converge to an optimal solution [6]. This leads to beam misalignment and degradation of the signal-to-interference-plus-noise ratio (SINR). In addition, the use of heavy matrix computations in real time creates peak loads on digital signal processors and FPGAs of base stations, thereby limiting the scalability of the system.

In recent years, a clear trend has emerged toward the application of artificial intelligence methods to physical-layer problems (Physical Layer AI) [11–13]. Deep learning techniques demonstrate impressive results in channel estimation and precoding tasks [14]. However, their use in mobile terminals and compact base stations is constrained by high computational complexity (the "curse of dimensionality") and the limited interpretability of decision-making processes (the "black-box" nature), which is unacceptable for mission-critical communication systems.

The objective of this work is to improve the efficiency of adaptive beamforming in the McWiLL system by developing a method for computing the weighting coefficients of the "Korona" antenna array based on ensemble machine learning techniques, specifically the Random Forest (RF) algorithm [15].

The research hypothesis is that replacing direct matrix computations with a predictive model based on an ensemble of decision trees will reduce the beam adaptation time by a factor of three to four while maintaining an acceptable level of sidelobe suppression. The RF algorithm possesses inherent parallelism and can be reduced to a set of logical comparison operations, which makes it well suited to the architecture of modern FPGAs used in McWiLL equipment.

The object of the research is space–time signal processing algorithms in professional mobile radio communication systems employing circular antenna arrays. The subject of the research is a methodology for applying supervised machine learning algorithms to approximate the optimal beamforming function under conditions of correlated interference and multipath signal propagation.

This work addresses the following tasks: the formation of training datasets that take into account the geometry of the "Korona" antenna array; the design of a decision forest architecture for regression of complex-valued weighting coefficients; and a comparative performance analysis of the proposed approach with conventional MVDR and LMS methods. The results of the study are intended to substantiate the feasibility of modernizing the mathematical and algorithmic framework of McWiLL base stations in order to support high-speed mobility scenarios and ensure reliable operation in complex interference environments.

2. Materials and Methods

2.1. Architecture of the McWiLL Physical Layer and Features of the "Korona" Antenna System

Broadband wireless access systems based on the McWiLL standard, also known under the international designation ITU-R M.1801-2 [16], occupy a unique niche in the spectrum of telecommunication technologies. Unlike mass-market cellular standards such as LTE and 5G NR, which are primarily focused on maximizing peak data rates, the McWiLL architecture is optimized to ensure reliability, high interference immunity, and wide coverage radius. These characteristics are critically important for Professional and Land Mobile Radio (PMR/LMR) communication networks.

The foundation of the physical layer of the system is CS-OFDMA technology. It combines the advantages of orthogonal frequency division multiplexing (OFDM) and code division multiple access (CDMA). In McWiLL, each information symbol is spread over the time–frequency resource using dedicated spreading code sequences. This approach provides high processing gain and robustness against frequency-selective fading. However, the cost of enhanced interference protection is the requirement for precise synchronization and complex signal processing at the receiver.

A key element ensuring the spectral efficiency of McWiLL is the use of adaptive antenna systems (Smart Antenna Systems, SAS). A base station (BTS) in a typical configuration is equipped with an 8-element circular antenna array known as the "Korona." Unlike a Uniform Linear Array (ULA) used in sectorized LTE antennas, a Uniform Circular Array (UCA) exhibits azimuthal symmetry, which makes it possible to form narrow radiation beams in any direction ($0^\circ \ldots 360^\circ$) without gain degradation at sector boundaries.

The geometry of the "Korona" array determines the specifics of the associated mathematical processing. While in a linear array the phase progression depends linearly on the side of the angle of arrival, in a circular array this relationship exhibits a more complex trigonometric form. This imposes stricter requirements on direction-of-arrival (DoA) estimation algorithms and beamforming procedures. The task of the smart antenna controller is to compute, in each time slot, complex weighting coefficients $w_1, \ldots, w_8$ based on the received pilot symbols, ensuring coherent combining of signals from the subscriber terminal (CPE) and destructive interference (nulling) of interfering signals.

2.2. Mathematical Model of Signals in a Circular Antenna Array

To formalize the adaptation problem, a mathematical model of the receive chain of a McWiLL base station is considered. The antenna array consists of M = 8 isotropic radiating elements uniformly distributed along a circle of radius R.

The McWiLL system employs CS-OFDMA broadband access technology. However, for the mathematical description of spatial filtering algorithms, it is appropriate to apply the "narrowband assumption," since OFDM signal processing is performed in the frequency domain, where the wideband signal spectrum is divided into multiple orthogonal subcarriers. Within the bandwidth of a single subcarrier, the signal envelope varies slowly compared to the time required for the wavefront to propagate across the antenna aperture.

Within this approximation, an array with M elements is considered, which is capable of suppressing up to K < M interference sources [17]. The first signal $s_0(t)$ is considered the desired signal (originating from the served subscriber), while the remaining $K - 1$ signals $s_k(t)$ represent active interferers. The numerical experiments emphasize K = 1 or K = 2 strong interferers because this is the representative McWiLL co-channel scenario.

The vector of signals at the outputs of the antenna elements $x(t) \in \mathbb{C}^{M\times 1}$ at time t is described by the classical equation:

$$x(t) = A(\theta)s(t) + n(t) \tag{1}$$

where

- $s(t) = [s_0(t), s_1(t), \ldots, s_{K-1}(t)]^T$—the vector of complex envelopes of source signals;
- $n(t) \sim \mathcal{CN}(0, \sigma_n^2 I)$—the vector of additive white Gaussian noise with zero mean and covariance matrix $\sigma_n^2 I$;
- $A(\theta) = [a(\theta_0), a(\theta_1), \ldots, a(\theta_{K-1})]$—the array manifold matrix, which defines the spatial response of the antenna array;
- Superscript T denotes ordinary transpose.

For a UCA located in the XY plane, the phase shift of the m-th element relative to the array center for a signal arriving from azimuth angle θ and elevation angle φ is given by the following expression:

$$\psi_m(\theta) = kR\cos(\theta - \gamma_m) \tag{2}$$

where $k = \frac{2\pi}{\lambda}$ denotes the wavenumber, λ is the wavelength, and $\gamma_m = \frac{2\pi(m-1)}{M}$ represents the angular position of the m-th array element.

Therefore, the control vector $a(\theta)$ takes the following form:

$$a(\theta) = \left[e^{j\psi_0(\theta)}, e^{j\psi_1(\theta)}, \ldots, e^{j\psi_{M-1}(\theta)}\right]^T \tag{3}$$

Unlike linear arrays, where the Vandermonde structure enables the use of fast algorithms such as Root-MUSIC, the structure $a(\theta)$ for a UCA does not exhibit rotational invariance in an explicit form (without prior transformation into phase modes). This significantly complicates the application of classical high-resolution spectral estimation methods.

The most important statistical characteristic of the received signal used in adaptation algorithms is the spatial covariance matrix R_{xx} [18]:

$$R_{xx} = E[x(t)x^H(t)] = AR_{ss}A^H + \sigma_n^2 I \tag{4}$$

where $R_{ss} = E[s(t)s^H(t)]$ is a source covariance matrix, H denotes Hermitian transpose (conjugate transpose).

In the case of uncorrelated sources, R_{ss} is a diagonal matrix. However, under multipath propagation conditions typical of urban environments, signals from a single source arrive from multiple directions with correlated phases. This results in a rank deficiency of the matrix R_{ss} and leads to a degradation in the performance of many conventional algorithms.

2.3. Formulation of the Optimal Beamforming Problem

The objective of adaptive beamforming (digital beamforming) is to synthesize a weighting vector $w = [w_1, \ldots, w_M]^T$ such that, through a linear combination of the input signals $y(t) = w^H x(t)$, it maximizes the signal-to-(noise plus interference) ratio, i.e., the SINR [19].

Mathematically, this problem reduces to minimizing the output power of the array subject to the constraint of maintaining a fixed gain in the direction of the desired signal θ_0 [20]:

$$\min\nolimits_{\mathrm{w}} E[|y(t)|^2] = \min\nolimits_{\mathrm{w}} w^H R_{xx} w \tag{5}$$

On the condition that $w^H a(\theta_0) = 1$.

This is the classical formulation of the MVDR problem, also known as the Capon solution. The method of Lagrange multipliers yields an analytical solution to this problem:

$$w_{MVDR} = \frac{R_{xx}^{-1} a(\theta_0)}{a(\theta_0)^H R_{xx}^{-1} a(\theta_0)} \tag{6}$$

The vector w_{MVDR} provides theoretically optimal interference suppression for Gaussian processes. The depth of the nulls in the radiation pattern depends on the accuracy of the estimation of the matrix R_{xx} and on the number of degrees of freedom of the array.

2.4. Critical Analysis of Classical Adaptation Algorithms

Despite the existence of a rigorous analytical solution, the practical implementation of the MVDR algorithm in real-time systems such as McWiLL is associated with several fundamental difficulties.

Direct computation of the MVDR weight vector w_{MVDR} requires the covariance matrix of the received array data R_{xx}. In practice, the true covariance matrix is unknown, and it is replaced by its finite-sample estimate, namely the sample covariance matrix (SCM), denoted by $\hat{R}_{xx}$ [21]:

$$\hat{R}_{xx} = \frac{1}{N} \sum_{n=1}^{N} x(t_n) x^H(t_n) \tag{7}$$

where N is the number of temporal snapshots.

Thus, in practical MVDR implementation, the ideal covariance matrix R_{xx} in the analytical solution is replaced by the sample estimate $\hat{R}_{xx}$. The computation of the weight vector then requires either inversion of $\hat{R}_{xx}$ or, equivalently, the solution of a system of linear equations using Cholesky or QR decomposition. The computational complexity of this operation is on the order of $O(M^3)$. For M = 8, this may not appear critical; however, in Massive MIMO systems with M = 64 or M = 128, the complexity grows cubically. Moreover, this operation must be performed for each frequency subcarrier or group of subcarriers, i.e., for each resource block, within every McWiLL frame interval of approximately 5–10 ms. This creates a substantial computational load on the DSP processors and FPGA resources of the base station, increasing both power consumption and hardware cost.

An alternative to matrix-based methods is provided by iterative algorithms. The LMS algorithm updates the weights according to the gradient descent rule:

$$w(n+1) = w(n) + \mu x(n) e^*(n) \tag{8}$$

where

- μ is the LMS step size controlling the adaptation rate;
- $e(n)$ denotes the error between the reference and the received signal;
- $(\cdot)^*$ denotes complex conjugation.

The main drawback of the LMS algorithm is that its convergence speed depends on the spread of the eigenvalues of the correlation matrix (the condition number). In the presence of strong interference, the eigenvalues R_{xx} differ significantly, and the descent trajectory becomes zigzag-shaped, which slows down convergence. The RLS (Recursive Least Squares) algorithm converges faster ($O(M^2)$), but it is computationally more complex and potentially unstable when implemented using fixed-point arithmetic, which is typical for FPGA-based systems.

In dense urban environments (urban canyons), which are characteristic of McWiLL network deployments, multipath propagation effects are observed, where coherent copies of the signal arrive at the antenna from different directions. Classical subspace-based algorithms MUSIC and adaptive methods MVDR interpret coherent signals either as a single source with a modified steering vector or suffer from signal subspace rank deficiency. This leads to the signal cancellation phenomenon, in which the adaptive array erroneously suppresses the direct path as interference relative to a reflected path. To mitigate this effect, spatial smoothing techniques are commonly used; however, they are effective mainly for linear equidistant arrays and cannot be directly applied to the circular "Korona" geometry without complex transformations.

The limitations of deterministic algorithms described above motivate a shift in the paradigm of smart antenna control. The task of mapping "input signal statistics → optimal weighting coefficients" can be formulated as a problem of approximating a multidimensional function.

Machine learning methods make it possible to transfer computational complexity from the execution stage (online inference) to the preliminary training stage (offline training).

Why Random Forest? Unlike deep neural networks, which require millions of multiply–accumulate (MAC) operations to propagate signals through multiple layers, the RF algorithm is based on a hierarchical structure of decision rules of the "IF–THEN" type:

1. Nonlinearity: RF is capable of efficiently approximating complex nonlinear decision boundaries in the feature space, which arise due to the trigonometric dependencies inherent in circular antenna arrays.
2. Noise robustness: Owing to the principles of bagging (bootstrap aggregation) and averaging over multiple decision trees, RF is less sensitive to measurement outliers and channel estimation errors than single decision trees or noise-sensitive methods such as MUSIC.
3. Hardware efficiency: Implementing RF on FPGA hardware reduces to a set of comparators and multiplexers, allowing the computation of weighting coefficients within only a few system clock cycles and achieving microsecond-level latency. This enables adaptive beamforming to be performed in every McWiLL frame time slot even on relatively low-cost hardware platforms.

Thus, the application of ensemble ML methods appears to be a well-founded approach for overcoming the bottlenecks of classical adaptive antenna theory in the context of modern requirements for professional radio communication systems.

2.5. Justification for Selecting the Random Forest Method for Physical Layer Tasks

The transition from deterministic algorithms (MVDR, MUSIC) to machine learning (ML) methods requires careful selection of the model architecture. In the context of the physical layer (PHY) of the McWiLL system, implemented on FPGA and digital signal processor (DSP) platforms, the key criteria include not only approximation accuracy, but also deterministic execution time (latency) and hardware resource efficiency.

The traditional approach to applying artificial intelligence to beamforming tasks involves the use of deep neural networks or convolutional neural networks (CNNs) [22]. However, despite their strong approximation capabilities, these models have several disadvantages in the context of the problem considered:

1. Computational redundancy: The forward pass (inference) of a fully connected neural network requires thousands of MAC operations. This is efficient on GPUs but costly on FPGA platforms with a limited number of DSP blocks.
2. Interpretability issues: The weighting coefficients of neural networks do not have a direct physical interpretation, which complicates error diagnosis (for example, in the case of communication failure in mission-critical scenarios).
3. Sensitivity to data scaling: Neural networks require careful normalization of input data, which complicates preprocessing of signals with a wide dynamic range (up to 90 dB in professional radio communication systems).

In this work, an alternative approach is proposed based on the RF algorithm. RF is an ensemble of decision trees trained independently using bootstrap aggregating (bagging) and random subspace methods.

Mathematically, the RF model for the regression problem (predicting the antenna weighting coefficients) can be expressed as the average prediction of N_{est} trees:

$$\hat{f}(x) = \frac{1}{N_{est}} \sum_{b=1}^{N_{est}} T_b(x) \tag{9}$$

where $T_b(x)$ is the output of the b-th tree for the input feature vector x.

Advantages of this approach for McWiLL smart antennas include the following:

Hardware efficiency: The structure of a decision tree is reduced to a set of hierarchical conditional operators (if–else). At the hardware level, this is implemented through comparators and multiplexers, without requiring the use of scarce hardware multipliers.

Resistance to overfitting: Due to averaging the decisions of multiple trees, random outliers in the training dataset (caused by impulsive interference) are compensated, reducing the variance of the weight vector estimation.

Operation with complex geometry: RF effectively partitions the nonlinear feature space formed by the circular geometry of the "Korona" antenna into local subregions, in each of which the approximation of the weights by a constant is acceptable.

One of the critical stages in developing an ML algorithm for radio systems is transforming complex signal samples into a real-valued feature vector suitable for input to decision trees.

Raw signal samples at the outputs of antenna elements $x(t) \in \mathbb{C}^{M\times 1}$ contain information not only about the spatial position of the sources, but also about the instantaneous carrier phase and modulation, which act as "noise" for the Direction of Arrival (DoA) estimation task.

To suppress this instantaneous dependence and extract stable spatial information, the received samples are first converted into the $\hat{R}_{xx}$, previously defined in (7). In the present feature extraction stage, this estimate is computed over Np pilot symbols in the McWiLL frame preamble, so that N = Np in (7).

The resulting matrix $\hat{R}_{xx}$ has dimension $M \times M$ and is Hermitian ($R = R^H$). This means that the diagonal elements are real (channel powers), while the elements of the lower triangle are complex conjugates of the elements of the upper triangle. Using all M^2 elements is redundant.

The feature vector $\mathcal{F} \in \mathbb{R}^D$ is constructed from non-redundant elements of upper triangular part of the $\hat{R}_{xx}$.

For the "Korona" antenna with M = 8 elements, the procedure is as follows:

Power: M values R_{ii}. They characterize the signal and noise level in each channel, which is important for detecting faulty elements or non-uniformity of the radiation pattern.

Phase shifts: $M(M-1)/2$ unique complex values R_{ii} $(i < j)$. These elements carry the key information about phase differences that determine the DoA.

Since Random Forest operates with real numbers, each complex element $R_{ij} = a + jb$ is split into two features: $\mathrm{Re}(R_{ij})$ and $\mathrm{Im}(R_{ij})$.

The final feature vector has the form:

$$\mathcal{F} = [R_{11}, \ldots, R_{MM}, \mathrm{Re}(R_{12}), \mathrm{Im}(R_{12}), \ldots, \mathrm{Re}(R_{M-1,M}), \mathrm{Im}(R_{M-1,M})]^T \tag{10}$$

The dimension of the feature space D is calculated as

$$D = M + 2 \times \frac{M(M-1)}{2} = M^2 \tag{11}$$

For an 8-element antenna, D = 64. This is a relatively small dimensionality, which makes it possible to train the model without applying dimensionality reduction methods such as Principal Component Analysis (PCA), while preserving all information about the correlation relationships.

The input data are preliminarily normalized according to the following rule in order to make the model invariant to the absolute level of the received power, which may vary due to the operation of the Automatic Gain Control (AGC):

$$\mathcal{F}_{norm} = \frac{\mathcal{F}}{\mathrm{trace}(\hat{R}_{xx})} \tag{12}$$

The antenna adaptation problem can be formulated in two ways: as classification (selecting a beam from a fixed codebook) or as regression (direct computation of the weights). For the McWiLL system, which requires deep interference suppression, the discreteness of a codebook is insufficient. Precise weight computation is required in order to form a “null” in an arbitrary direction. Therefore, a multidimensional regression problem is solved.

A single decision tree T_b is constructed by recursively partitioning the feature space. At each node, a feature f_k from the vector $\mathcal{F}$ and a threshold t are selected for Mean Squared Error (MSE) after the split:

$$L(k,t) = \frac{1}{N_L}\sum_{i\in\mathrm{Left}} ||\mathrm{y}_i - \overline{\mathrm{y}}_L||^2 + \frac{1}{N_R}\sum_{j\in\mathrm{Right}} ||\mathrm{y}_j - \overline{\mathrm{y}}_R||^2 \tag{13}$$

where y—the target vector of weight coefficients, $\overline{\mathrm{y}}_{L,R}$—the mean value of the vector in the left and right child nodes.

The target vector y has dimension $2M$ (real and imaginary parts of the weights $w_1, \ldots, w_8$). A distinctive feature of our implementation is the use of Multi-Output Random Forest: each tree stores not a single value in its leaves, but a vector of length 16. This allows the phase relationships between the antenna elements to be preserved within a single model, which is critically important for beamforming.

Because all 16 outputs share one tree structure, the split in each node minimizes the total MSE summed over the components (Equation (13)), which keeps the predicted real and imaginary parts mutually consistent.

2.6. Specifics of Implementation on the McWiLL Hardware Platform

The proposed method was developed with consideration of its potential integration into the existing hardware architecture of McWiLL base stations employing “Korona” smart antenna systems. The main requirement for such an implementation is to provide low and deterministic latency in the computation of beamforming weights, since the radiation pattern must be updated within the frame timing structure without disrupting signal reception and processing procedures. At the same time, the method must preserve the interference suppression capability of classical adaptive beamforming approaches by forming sufficiently deep nulls in the directions of active interferers while maintaining the desired signal gain.

Before deployment on the FPGA, the Random Forest model is trained offline using synthetically generated channel realizations corresponding to the geometry of the “Korona” antenna array. In the training data generator, the steering vectors are formed with allowance for mutual coupling between antenna elements. If C denotes the mutual coupling matrix, the effective steering vector used in the training-data generator is written as

$$\widetilde{a}(\theta) = Ca(\theta) \tag{14}$$

where $a(\theta)$ is the ideal steering vector of the antenna array corresponding to the signal arrival angle θ.

For each generated channel scenario, the reference beamforming vector is calculated using the analytical MVDR solution based on the true covariance matrix rather than its finite-sample estimate. Since the Random Forest operates with real-valued outputs, the complex optimal weight vector is represented as a 16-component target vector containing its real and imaginary parts:

$$y_i = [\mathrm{Re}(w_{opt}), \mathrm{Im}(w_{opt})] \tag{15}$$

The offline training procedure, which sweeps the operating SNR and INR ranges, is summarized in Algorithm 1.

Algorithm 1. Offline training of the multi-output RF-MVDR model.

Input: array geometry (M, R, coupling matrix C); the scenario distribution; the number of training realizations S.
Output: a trained multi-output Random Forest of 50 regression trees.
For each training realization:

1. Draw a scenario–the desired and interfering directions and the SNR/INR from the operating distribution.
2. Generate the snapshots–N array snapshots from the narrowband signal model of Section 2.2, with mutual coupling included (Equation (14)).
3. Form the feature vector–estimate the sample covariance matrix (Equation (7)) and build the normalized feature vector (Equations (10)–(12)).
4. Form the target label–compute the reference weights from the analytical MVDR solution on the true covariance (Equation (6)), encoded as the real/imaginary label vector (Equation (15)).

Train a single multi-output Random Forest on the feature-label pairs (MSE split, 50 trees, minimum 5 samples per leaf).

After training, the tree structure, split thresholds, feature indices, and lead payloads are converted to a fixed point and mapped to on-chip BRAM. In online inference, the weight vector is computed during the guard period of the uplink slot. The corresponding online inference procedure is given in Algorithm 2.

Algorithm 2. Online inference on the FPGA.

Input: the pilot-window snapshots; the trained forest in BRAM (Q4.12/Q2.14).
Output: the complex weight vector w.

1. Form the feature vector–estimate the sample covariance matrix from the pilot symbols (Equation (7)) and build the normalized feature vector (Equations (10)–(12)) in Q4.12.
2. Traverse the forest–pass the feature vector to the 50 trees; each traversal is a sequence of threshold comparisons only, returning a stored lead weight vector (Q2.14). For synthesis, the trees are pruned to depth 12 (MinLeafSize = 50).
3. Aggregate–average the lead vectors (Equation (9)) and assemble the complex weights from their real and imaginary parts.
4. Apply w in the beamformer.

The weights-computation core uses only comparisons and memory reads.

For comparative evaluation of the computational properties of the proposed approach, the classical MVDR algorithm, the iterative LMS/NLMS and RLS algorithms, and a neural-network model based on a multilayer perceptron (MLP) were considered together with RF-MVDR. These methods are widely used in adaptive beamforming tasks and make it possible to compare the proposed approach with existing solutions both in terms of radiation pattern formation quality and computational cost. Detailed quantitative comparison results are presented in the experimental section, whereas this subsection focuses primarily on the specifics of their hardware implementation.

The computational complexity of a single weight-vector update was evaluated for all considered methods.

MVDR. The MVDR algorithm requires approximately $\sim O(M^3)$ floating-point operations due to Cholesky factorization and two triangular solves. In addition, it involves division and square-root operations, which are computationally expensive for FPGA implementation.

RLS. The RLS algorithm requires approximately $\sim O(M^2)$ operations per update, as well as one division operation. It also requires multiple iterations before convergence is achieved.

LMS (NLMS). The LMS/NLMS algorithm requires approximately $\sim O(M)$ multiply–accumulate operations per sample. It is the least computationally demanding among the iterative methods, but it is characterized by relatively slow convergence.

Multilayer-perceptron baseline (MLP). For a network with two hidden layers of 64 neurons each, the forward pass requires $64 \times 64 + 64 \times 64 + 64 \times 16 \approx 9200$ MAC operations.

Random Forest. The complexity of a single tree is $O(D_{\max})$. For the entire ensemble, the complexity is $N_{\text{est}} \times D_{\max}$ comparison operations and $N_{\text{est}} \times 2M$ addition operations. For $N_{\text{est}} = 50$ and $D_{\max} = 12$, this corresponds to 600 comparisons and 800 additions, with no multiplication operations involved except for the final normalization.

Thus, the computational complexity of the proposed method depends linearly on the tree depth and the number of trees and does not involve computationally intensive linear algebra operations. This property makes the tree-based structure naturally suitable for implementation using LUT-based comparators and BRAM tables. The synthesizable Random Forest core was described in MATLAB 2023b, converted into Verilog using MATLAB HDL Coder, and synthesized in Xilinx Vivado 2024.1 for a Kintex-7 FPGA representing the class of platforms used in McWiLL equipment (NIRIT-XINWEI Telecom Technologies Ltd. (NXTT), Odesskaya St., 2c, Moscow 117638, Russia). Quantitative results on hardware resource utilization and inference latency are presented in Section 3. The proposed Random Forest-based approach for controlling the "Korona" smart antenna provides a balanced compromise between the theoretically optimal but computationally demanding MVDR algorithm and the real-time requirements imposed on practical communication systems.

3. Results

3.1. Software Implementation and Experimental Parameters

To verify the proposed methodology for adaptive control of the "Korona" antenna array, a comprehensive simulation model was developed in MATLAB R2023b using the Phased Array System Toolbox. The Random Forest regression model was trained with the Statistics and Machine Learning Toolbox and the MLP with the Deep Learning Toolbox. The synthesizable hardware core was described in MATLAB 2023b, converted to Verilog with HDL Coder, and synthesized in Xilinx Vivado 2024.1; a bit-exact functional co-simulation of the generated RTL against the fixed-point software reference was carried out in Aldec Active-HDL 12.

The proposed RF-MVDR is compared with the classical MVDR, the RLS algorithm, the normalized LMS, and a MLP approach. Note that the LMS and RLS baselines are driven by a steering-vector-projection reference, which reflects the configuration actually used in the deployed system; this choice–rather than any convergence failure or unfair setup–is what limits their steady-state SINR to the plateau values reported in Section 3.4.1.

The physical-layer parameters follow the McWiLL specification (ITU-R M.1801) and the NIRIT-SINVEY equipment documentation:

- Antenna system: 8-element uniform circular array (UCA);
- Array radius: $R = 0.5\lambda$;
- Element radiation pattern: isotropic;
- Signal structure: CS-OFDMA, 5 MHz channel bandwidth;
- Sources: 1 signal of interest (SOI) at 0° + 2 interferers at ±60°;
- Interference-to-noise ratio (INR): 20 dB;
- Signal-to-noise ratio (SNR): from −10 to +30 dB;
- Number of snapshots: N = 32 (frame preamble).

Robustness was additionally assessed for a low snapshot count (N = 16 = 2M), coherent multipath (a coherence sweep). The target FPGA is a Xilinx Kintex-7 xc7k325t-2 (203,800 LUT, 407,600 FF, 840 DSP48, 445 BRAM36); the core features and thresholds use signed Q4.12 format, and the output weights use Q2.14.

3.2. Random Forest Model Configuration

Based on the methodology described earlier, a multi-output regression forest model was trained with the following hyperparameters:

- Number of trees N_{est}: 50.
- Splitting criterion: MSE.
- Minimum number of samples in a leaf: 5 (to smooth measurement noise).
- Input features: 64 elements (real and imaginary parts of the covariance matrix 8 × 8).
- Outputs: 16.
- Training dataset: 80,000 samples.
- Test dataset: 20,000 samples (non-overlapping with the training set).

3.3. Analysis of Beam Pattern Formation Accuracy

As a first step, it was verified whether the trained RF-MVDR model reproduces the angular selectivity of the classical MVDR beamformer in a baseline scenario with well-separated desired and interfering directions. This case serves as a reference check: the interferers lie far outside the main lobe, so deep nulls are formed without distorting the main steering direction.

Figure 1 shows the normalized radiation patterns of the eight-element "Korona" circular antenna array for the case where the desired signal (SOI) arrives from 0° while two strong interferers arrive from ±60°. The solid blue curve corresponds to the classical MVDR solution, whereas the red dashed curve represents the proposed RF-MVDR approach.

The pattern was obtained using a narrowband spatial model for one CS-OFDMA subcarrier and a uniform circular array of M = 8 isotropic elements; mutual coupling was taken into account through the effective steering vector (Equation (14)). For MVDR, the interference-plus-noise covariance matrix was estimated using the known pilot signal with diagonal loading; RF-MVDR used the same input statistics but predicted the weight vector from covariance-matrix features without matrix inversion.

Both algorithms form the main lobe toward the SOI (0°) with maximum gain and deep nulls toward the interferers at ±60°: MVDR reaches a depth of about −44 dB and RF-MVDR about −33 dB. The red RF-MVDR curve closely follows the blue MVDR curve, including the side-lobe structure, which confirms that the trained model reproduces the classical radiation pattern without any matrix-inversion operations. Because the ±60° interferers lie well outside the main lobe, the nulls are formed without distorting it, and the SOI remains at the pattern peak.

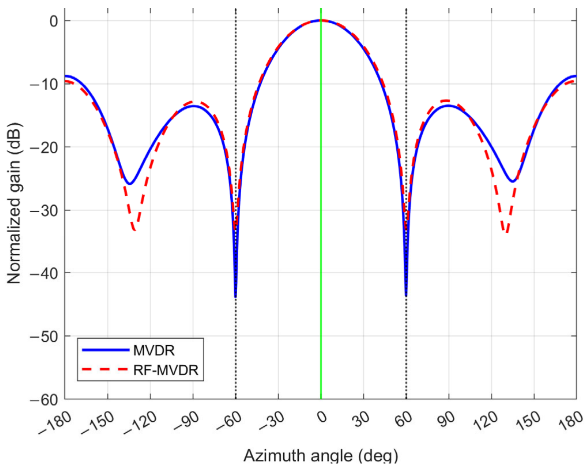

Figure 1. Normalized radiation patterns of MVDR and RF-MVDR for a signal of interest (SOI) at 0° and two interferers at ±60°, with $N = 32$ snapshots. The solid blue curve is MVDR and the red dashed curve is RF-MVDR; the vertical green line marks the SOI direction and the vertical black dotted lines mark the two interferer directions.

The next stage of the analysis was aimed at verifying whether the trained RF-MVDR model can reproduce the angular selectivity of the classical MVDR beamformer in a challenging close-interference scenario. In contrast to the previous simulations with well-separated desired and interfering directions, this test considers a small angular separation between the desired signal and the interference source. Such a configuration is important because it evaluates not only the average interference suppression capability of the method, but also its ability to form a narrow adaptive null in the vicinity of the desired signal direction.

Figure 2 shows the normalized radiation patterns of the eight-element "Korona" circular antenna array for the case where the desired signal arrives from 25°, while a strong interferer arrives from 30°. Thus, the angular separation between the SOI and the interferer is only 5°. This value defines a stress-test scenario in which the interferer is located inside the main-lobe region of the compact circular array. The solid blue curve corresponds to the classical MVDR solution, whereas the red dashed curve represents the radiation pattern obtained using the proposed RF-MVDR approach.

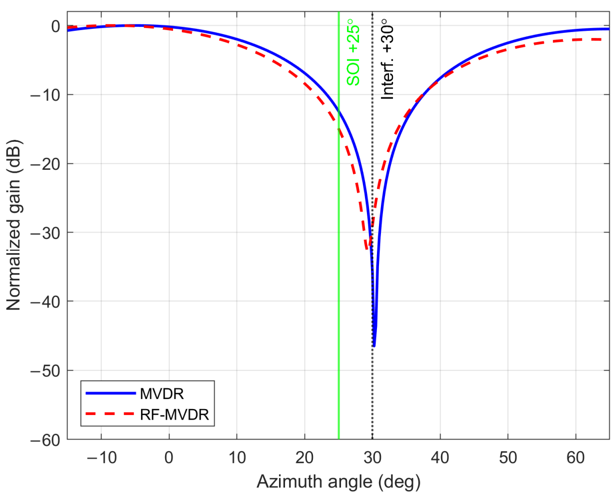

Figure 2. Normalized radiation patterns of MVDR and RF-MVDR in a close SOI-interferer scenario with 5° angular separation.

In the considered case, MVDR forms a null in the interferer direction (30°) with a depth of about −34 dB, whereas RF-MVDR provides a null of about −29 dB while preserving a similar radiation-pattern shape. At the same time, the SOI direction appears below the pattern maximum (by about 12 dB), which is caused by the need to place the null only 5° away from the desired signal. Thus, this example illustrates a limiting case of closely spaced SOI and interference directions, rather than a typical angular separation used for training-set generation.

The radiation-pattern analysis is complemented by an evaluation of robustness to array-model mismatch. Figure 3 shows the dependence of the array gain on the angle of arrival (Y-axis: gain in dB; X-axis: angle in degrees) under model-mismatch conditions caused by 2° per-element phase errors. The vertical green line at 0° indicates the desired-signal direction, which serves as the primary steering direction for the receive beamformer; the vertical black dashed lines at ±60° mark the directions of the strong interferers, at which deep nulls are expected. The solid blue curve corresponds to the classical MVDR under the 2° phase error, whereas the red dashed curve represents the proposed RF-MVDR under the same phase error.

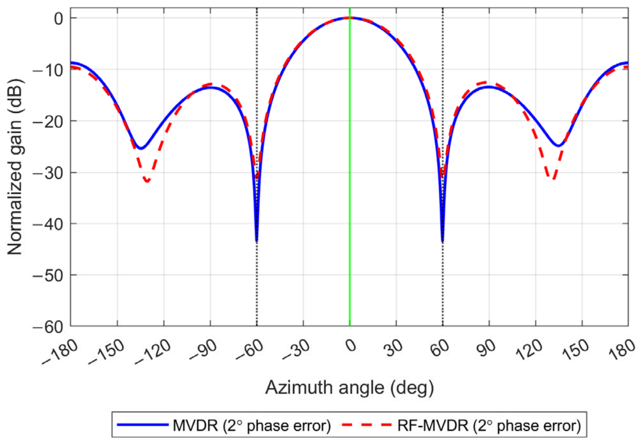

Figure 3. Robustness of the MVDR and RF-MVDR beamformers to 2° per-element phase distortions. The solid blue curve is MVDR and the red dashed curve is RF-MVDR, both under the same 2° phase error; the vertical green line marks the SOI direction (0°) and the vertical black dotted lines mark the interferer directions (±60°).

The proposed method demonstrates high robustness to array-model mismatch. Despite the 2° phase errors, the main lobe toward the desired signal is preserved and the nulls remain in the interferer directions ±60°: the classical MVDR reaches a null depth of about −43 dB and RF-MVDR about −31 dB. The red RF-MVDR curve closely follows the blue MVDR curve over the entire angular range, including the side-lobe structure, which confirms the robustness of the learned approach to phase distortions: the ensemble averaging over decision trees yields a "smoothed" weight vector that is less sensitive to calibration errors than the exact matrix-inversion solution.

3.4. Comparative Analysis of Output SINR, Convergence, and Robustness

In addition to the radiation-pattern analysis presented in Sections 3.1–3.3, the effectiveness of the proposed method was evaluated quantitatively in terms of the output SINR. The RF-MVDR approach was compared with the classical MVDR algorithm, RLS, NLMS, and MLP. All experiments were conducted under the common simulation conditions described in Section 3.1.

The evaluation covers five complementary aspects: the output SINR as a function of the input SNR for N = 32 snapshots; robustness under a reduced number of snapshots, N = 16; sensitivity to coherent multipath propagation; convergence behavior of the iterative algorithms; and the average radiation-pattern null depth in the interference directions as a function of SNR. The latter metric provides a direct link between the quantitative SINR analysis and the radiation-pattern results discussed in Sections 3.1–3.3.

3.4.1. Output SINR Versus Input SNR at N = 32 Snapshots

Figure 4 shows the output SINR as a function of the input SNR at N = 32 preamble snapshots for all considered methods. The desired signal arrives from 0° and two interferers from ±60°.

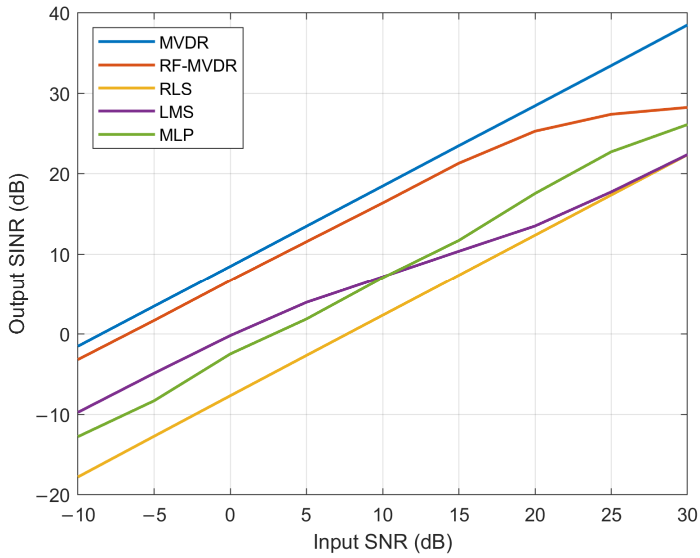

Figure 4. Output SINR versus input SNR (N = 32).

The classical MVDR serves as the benchmark and grows essentially linearly with SNR (with a slope of ≈ 1 dB/dB and an ≈ 9 dB offset due to the array gain). The proposed RF-MVDR closely follows MVDR over the operating SNR range: the gap is about 2 dB at low and moderate SNR (6.7 vs. 8.5 dB at SNR = 0 dB; 16.4 vs. 18.5 dB at SNR = 10 dB) and grows at high SNR, where the RF-MVDR curve saturates at about 28 dB (28.3 vs. 38.5 dB at SNR = 30 dB). This saturation results from the finite accuracy of the tree-ensemble weight approximation and from the feature normalization that removes the absolute received-power scale; over the typical McWiLL uplink operating range RF-MVDR remains within ≈2–3 dB of MVDR.

The iterative LMS and RLS algorithms, which use the steering-vector-projection reference (as deployed in the system), lie several decibels below the covariance-based methods across the whole range (RLS = 2.4 dB, LMS = 7.2 dB at SNR = 10 dB, against 16.4 dB for RF-MVDR), owing to interference and noise leakage into the reference signal; LMS exceeds RLS at low SNR because of its conventional-beamformer initialization. The MLP neural-network baseline is intermediate (7.1 dB at SNR = 10 dB) and remains below RF-MVDR throughout. Thus, RF-MVDR attains an SINR close to that of the classical MVDR and consistently outperforms the iterative LMS/RLS and the neural-network approach, while requiring no covariance-matrix inversion—which underlies its hardware advantages discussed in the following sections.

3.4.2. Performance at a Reduced Snapshots Count (N = 16)

To assess operation with a short training sequence, the experiment of Section 3.4.1 is repeated at N = 16 snapshots—the Reed–Mallett–Brennan threshold (N = 2M) at which sample-covariance methods lose about 3 dB relative to the known-covariance case. The geometry and conditions match previous sections. Results presented in the Figure 5.

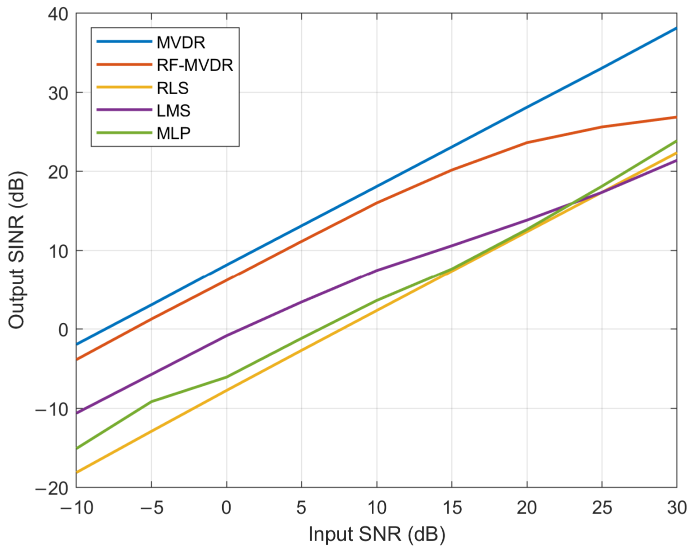

Figure 5. Output SINR versus input SNR at a low snapshot count N = 16 = 2M.

Despite halving the sample size relative to Section 3.4.1, the classical MVDR and the proposed RF-MVDR show virtually no degradation: at SNR = 10 dB, MVDR yields 18.1 dB (vs. 18.5 dB at N = 32) and RF-MVDR yields 16.0 dB (vs. 16.4 dB); at SNR = 30 dB, the corresponding values are 38.2 dB and 26.9 dB. The robustness of MVDR stems from the pilot-projected interference-plus-noise covariance estimate (Section 2.6), which remains well conditioned even at small N, while RF-MVDR predicts the weight vector directly from covariance features and is therefore likewise insensitive to the reduced sample size.

The iterative algorithms and the neural-network baseline fall markedly below the covariance-based methods, especially at low SNR: at SNR = 10 dB, LMS gives 7.5 dB, MLP 3.6 dB, and RLS 2.4 dB, whereas RF-MVDR provides 16.0 dB. Thus, RF-MVDR retains a performance close to MVDR with a preamble that is half as long, which is critical for high-mobility scenarios (e.g., communication with high-speed trains) where the training-sequence length is limited by the channel coherence time.

3.4.3. Robustness to Coherent Multipath Propagation

To assess robustness under realistic urban-multipath conditions, a scenario combining the typical base-station impairments is considered. In addition to the direct desired signal from 0°, a coherent copy of the same signal arrives from a random direction in the +20…+40° range (with a random copy amplitude), together with an independent co-channel interferer from +60°. Array calibration phase errors (2° per element) and DoA uncertainty (1°) in the steering vector of MVDR and RF-MVDR are additionally included. The iterative LMS and RLS algorithms use the known preamble pilot (training-based adaptation). The degree of coherence between the direct ray and the reflected copy is set by the coefficient ρ, which varied from 0 to 1. The resulting output SINR as a function of ρ is shown in Figure 6.

All methods are robust to coherence: none of the curves collapses as ρ grows. The proposed RF-MVDR attains the highest SINR over most of the range (about 16.8–16.9 dB) and degrades only slightly (by about 0.7 dB) due to the phase errors relative to the idealized conditions, remaining in the top group. The classical MVDR yields about 16 dB and is likewise robust. The pilot-aided LMS and RLS are competitive (about 14–15 dB at low ρ) and increase with coherence, reaching 17.7 and 17.9 dB at $\rho = 1$: a fully coherent copy carries correlated desired-signal energy that the pilot-based MMSE solution combines coherently (a diversity gain). The MLP neural-network baseline yields about 12 dB and decreases slightly with ρ (to 10.9 dB at $\rho = 1$).

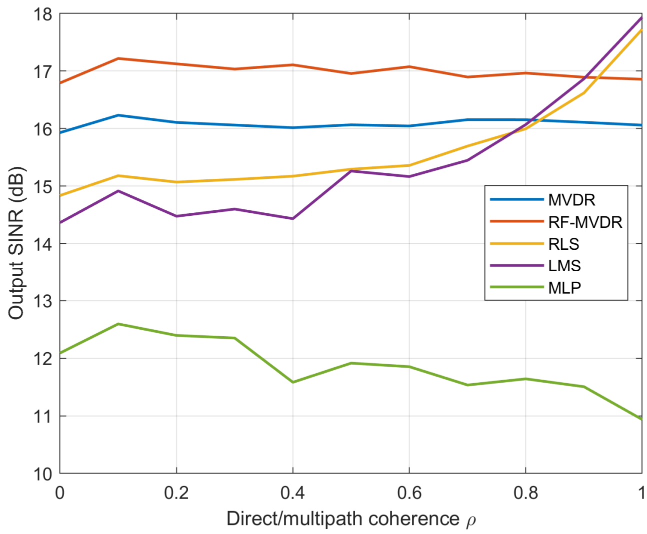

Figure 6. Output SINR versus the coherence coefficient ρ.

Thus, even under realistic array-model mismatch and when the iterative methods are provided with an ideal pilot reference, RF-MVDR remains robust to coherent multipath and remains among the best methods, which supports the suitability of the learned approach for urban McWiLL conditions.

3.4.4. Convergence Behavior of the Iterative Algorithms

Besides the achievable SINR, the adaptation speed is important for fast-varying channels. Figure 7 shows the output SINR as a function of the snapshot index at SNR = 10 dB within the frame preamble N = 32 snapshots. The iterative LMS and RLS algorithms are shown as convergence curves, whereas MVDR, RF-MVDR, and the MLP neural network appear as horizontal reference lines, since they form the weight vector in a single step from the statistics of one snapshot.

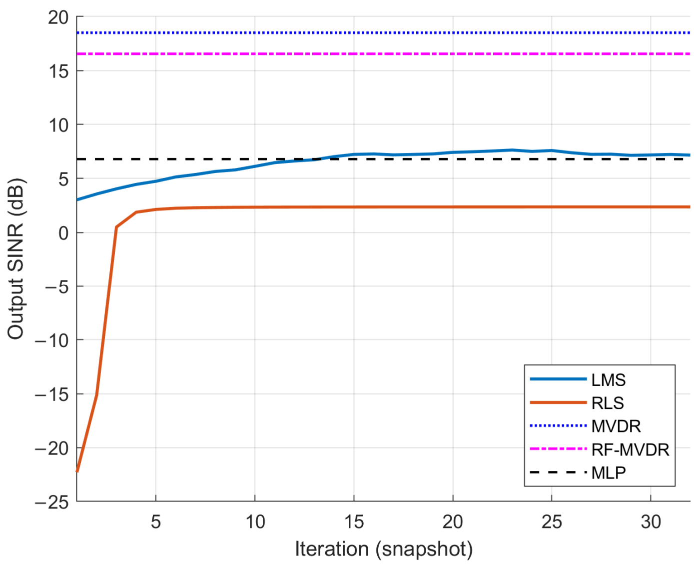

Figure 7. Convergence of algorithms.

RLS converges very quickly, reaching its steady-state level of about 2.4 dB within a few snapshots (about five). LMS adapts more slowly, reaching about 7 dB by ~15 snapshots and maintaining this level until the end of the preamble. Despite converging, both iterative methods remain substantially below the non-iterative solutions: MVDR provides 18.5 dB, RF-MVDR 16.6 dB, and the MLP neural network 6.8 dB, all three forming the weights without iterations (zero adaptation latency). The low steady-state level of LMS and RLS is due to the steering-vector-projection reference of the deployed system, not to the convergence rate itself.

This behavior is essential for McWiLL high-mobility scenarios: with a limited preamble length and a fast-varying channel, the iterative algorithms cannot reach a high SINR in time, whereas RF-MVDR produces a near-MVDR solution instantly, from the statistics of a single snapshot, enabling stable beamforming in every frame time slot.

3.4.5. Average Radiation-Pattern Null Depth Versus Input SNR

To link the quantitative SINR analysis (Sections 3.4.1–3.4.4) with the radiation patterns (Section 3.3), the average null depth toward the ±60° interferers relative to the desired-signal direction is evaluated as a function of the input SNR (Figure 8). The null depth is defined as the pattern gain toward the interferer normalized by the gain toward the SOI (in dB); a more negative value corresponds to deeper suppression. The conditions match Section 3.4.1 (N = 32, INR = 20 dB).

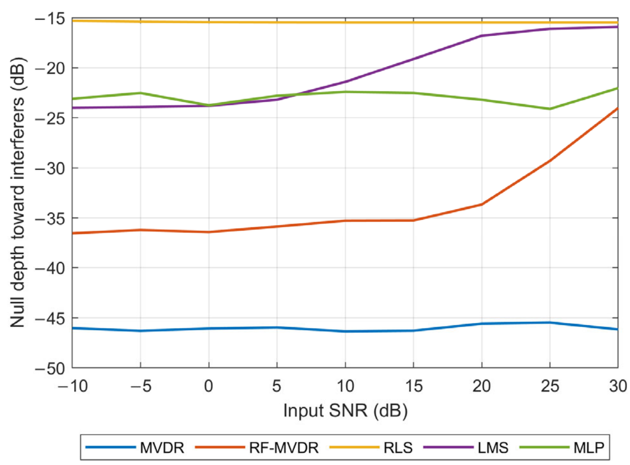

Figure 8. Average radiation-pattern null depth toward the ±60° interferers (relative to the SOI) versus input SNR.

The classical MVDR forms the deepest and most stable nulls—about −46 dB over the whole SNR range, owing to the pilot-projected covariance estimate (Section 2.6). The proposed RF-MVDR provides deep nulls ranging from −36 dB at low SNR to −24 dB at SNR = 30 dB; the gradual reduction in depth with increasing SNR is consistent with the SINR saturation observed in Section 3.4.1 and reflects the finite accuracy of the tree-ensemble weight approximation. Nevertheless, these values (24–36 dB) are sufficient to suppress the 20 dB INR interferers below the noise floor, and at the operating SNR = 10 dB, the RF-MVDR null depth is about −35 dB, in agreement with the polar and Cartesian radiation patterns of Section 3.3.

The iterative algorithms and the neural-network baseline form markedly shallower nulls: LMS from −24 to −16 dB (with depth decreasing as SNR increases), MLP about −22. . . −24 dB, and RLS about −15.5 dB (the shallowest, owing to the projection reference). Thus, the covariance-based methods (MVDR and RF-MVDR) achieve substantially deeper spatial interference suppression than the deployed iterative algorithms and the neural network, which reconciles the quantitative results of Section 3.4 with the radiation-pattern shapes of Section 3.3.

3.5. FPGA Implementation: Resource Utilization, Inference Latency, and Verification

3.5.1. Hardware Resource Utilization

The resources required by the weight-computation block are shown in Figure 9. The left panel reports the usage of DSP48 hardware multipliers—the scarcest resource—and the right panel reports the look-up tables (LUTs) and flip-flops (FFs).

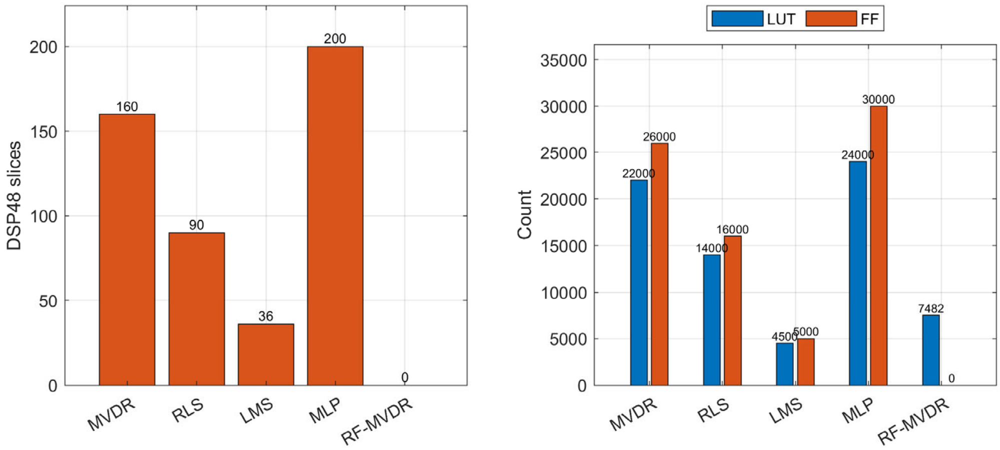

Figure 9. FPGA resource utilization per weight-computation block: (**left**) DSP48 hardware multipliers; (**right**) LUTs and flip-flops—for MVDR, RLS, LMS, MLP, and RF-MVDR.

The decisive result is seen in the left panel of Figure 9: RF-MVDR uses no DSP48 blocks at all—the decision-tree structure reduces to comparators and Block-RAM look-ups, with no multiply operations. For comparison, the classical MVDR requires about 160 DSP48 blocks (8×8 matrix inversion), the MLP neural network about 200 (a multiply–accumulate array), RLS about 90, and LMS about 36. The zero-multiplier consumption frees this scarce resource for other physical-layer tasks (FFT, channel coding). The HDL Coder report for the depth-12 core confirms the absence of multipliers: 0 multipliers, 42 adders/subtractors, 16 registers, 24 multiplexers, and 0 shifters.

The right panel of Figure 9 shows that RF-MVDR uses a moderate amount of fine-grained resources: 7482 LUTs and a negligible number of flip-flops (the core is combinational), which is fewer than MVDR (≈22,000 LUTs) and MLP (≈24,000 LUTs); the decision tree itself is stored in Block RAM. Thus, RF-MVDR moves the computation off the scarce hardware multipliers onto the abundantly available logic tables and memory, which underlies its hardware efficiency.

3.5.2. Inference Latency

Besides resource usage, the weight-vector computation latency is important for operation in every McWiLL frame time slot. Figure 10 shows the latency of a single weight update at a 200 MHz clock (5 ns clock period).

RF-MVDR achieves the lowest latency—3.0 μs. Since a forest of 50 trees of depth 12 issues one threshold comparison per clock, the number of cycles equals the number of operations: $50 \times 12 = 600$ cycles, which at 5 ns/cycle gives 3.0 μs. The classical MVDR requires 12.3 μs: computing w via Cholesky factorization takes on the order of 680 operations, but the actual latency exceeds the operation count because each complex floating-point multiplication is multi-cycle, the division and square-root cores have a long latency on the critical path, and the Cholesky recursion is inherently sequential; at an effective ~3.6 cycles per operation, this amounts to about 2460 cycles. Therefore, RF-MVDR is 4.1× faster than the classical MVDR (12.3/3.0 = 2460/600).

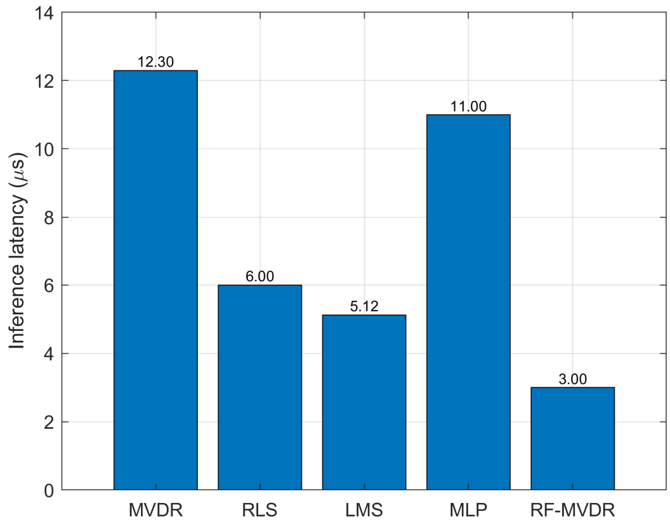

Figure 10. FPGA inference (weight-vector computation) latency at 200 MHz.

The remaining methods are intermediate: the MLP neural network at 11.0 μs (~9200 multiply–accumulate operations under time-multiplexing), RLS at 6.0 μs, and LMS at 5.12 μs. The advantage of RF-MVDR is obtained by replacing multi-cycle, sequential floating-point linear algebra (matrix inversion and division) with single-cycle, parallelizable integer comparisons, which enables microsecond-level adaptation in every frame.

3.5.3. Bit-Exact Functional Verification of the Synthesized Core

To confirm that the deployed hardware core introduces no inference error beyond the documented quantization, the synthesizable tree-inference core was verified by bit-exact co-simulation against the fixed-point software reference.

The synthesizable function produces reference integer output codes (Q2.14 format) for eight quantized feature vectors, using the same fixed-point constants from which the HDL was generated. A self-checking testbench applies the features to the 64 inputs, reads the registered outputs one clock cycle later, and compares them with the reference for each of the 16 components of each vector; the resulting functional simulation is shown in Figure 11. The design was compiled and simulated in Aldec Active-HDL 12. The result was that all $8 \times 16 = 128$ output samples match the MATLAB 2023b reference to the least significant bit (PASS for every vector). The corresponding full 16-component weight vector over the eight vectors is shown in Figure 12.

The waveforms in Figures 11 and 12 confirm the pipeline contract: the ce_out ready flag exactly replicates clk_enable (a one-cycle output-valid latency), the outputs are latched on the rising edge and held for the full clock cycle, and the 16-component weight vector is updated atomically in a single clock cycle when a different leaf is activated (Figure 12). Identical input vectors fall into the same leaf and produce identical outputs, which is visible in Figure 11 (vectors yielding the same $y_0 \ldots y_3$) and is the correct property of the piecewise-constant tree mapping.

Thus, the synthesized core is functionally equivalent to the fixed-point model bit-for-bit; combined with the single-cycle, multiplier-free datapath (Sections 3.5.1 and 3.5.2), this confirms the readiness of the RF-MVDR core for deployment in McWiLL equipment.

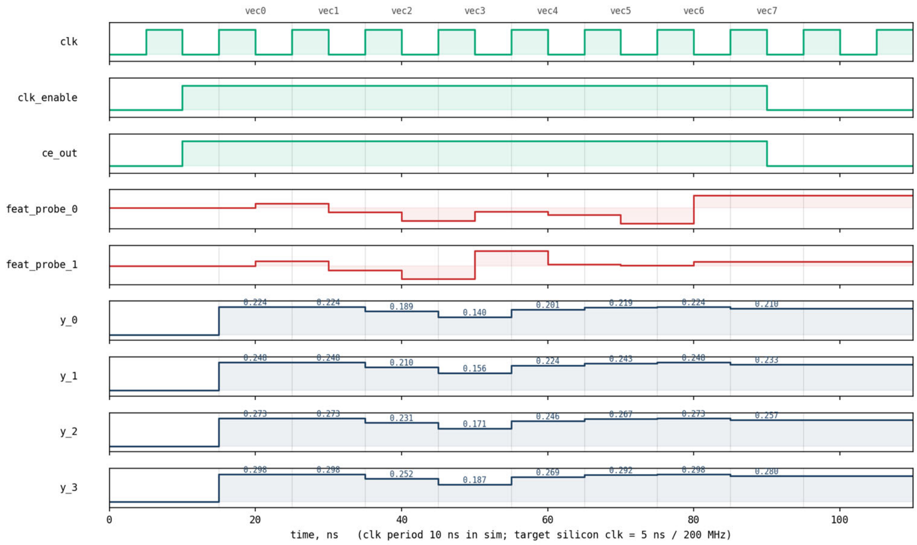

Figure 11. Functional simulation of the synthesized core in Aldec Active-HDL over the eight test vectors. Green traces are the clock and control signals (clk, the clk_enable strobe and the ce_out ready flag), red traces are the two feature probes, and dark blue traces are the output weight-vector components y0. . .y3; the numeric annotations above the blue traces give the corresponding real-valued weights.

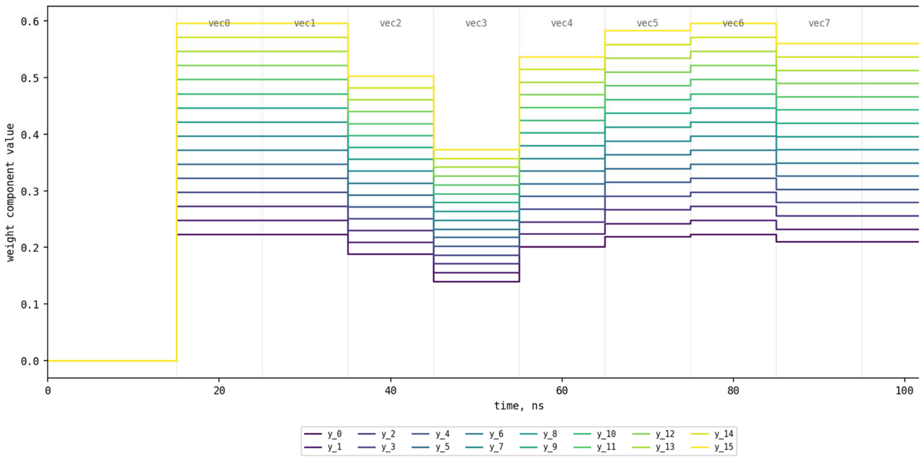

Figure 12. The full 16-component output weight vector $y_0 \ldots y_{15}$ (Q2.14 format) over time.

4. Discussion

The obtained results show that a learned model based on a Random Forest can reproduce the spatial selectivity of the classical MVDR algorithm while using a fundamentally different computational realization. The RF-MVDR radiation patterns virtually coincide with those of MVDR—both in the baseline scenario with deep nulls toward the ±60° interferers (Section 3.3) and under close angular spacing and phase errors—and in terms of output SINR, the method stays close to the classical MVDR over the operating signal-to-noise range (Section 3.4). At the same time, RF-MVDR requires neither covariance-matrix inversion nor iterative adaptation, which provides its principal advantages.

The comparative analysis reveals an accuracy–complexity trade-off. Over the McWiLL uplink operating range, RF-MVDR trails MVDR by no more than ≈2 dB in SINR; at very high SNR, a saturation near 28 dB appears, caused by the finite accuracy of the tree-ensemble weight approximation and the feature normalization. This small accuracy loss is offset by the gains in speed and hardware efficiency and is not limiting under typical operating conditions, where the SINR is determined primarily by interference suppression rather than by the ultimate gain.

Relative to the other adaptive methods, RF-MVDR shows a consistent advantage. The iterative LMS and RLS with the steering-projection reference used in the deployed system are limited by interference leakage into the reference signal and require time to converge, whereas RF-MVDR forms its solution instantly from the statistics of a single snapshot (Section 3.4.4)—critical for high-mobility scenarios with a short preamble. Compared with the neural-network baseline (MLP), the Random Forest is not only more economical in hardware resources but also more robust: at a low snapshot count and under multipath, RF-MVDR retains a high SINR, whereas the MLP degrades markedly. This is consistent with the nature of ensemble averaging (bagging), which produces a "smoothed" weight vector less sensitive to estimation errors, phase distortions, and correlated signal structure.

The handling of mutual coupling deserves separate attention. The dense layout of the "Korona" circular array leads to significant mutual coupling, and neglecting it in the classical methods (MVDR, MUSIC) causes substantial direction-of-arrival errors and requires online calibration and multiplication by the inverse coupling matrix. Since the Random Forest was trained on data that already include mutual-coupling effects, it compensates these distortions automatically, without additional computational blocks or a real-time calibration procedure; the node thresholds of the trees are tuned directly to the real (distorted) signal statistics.

From the implementation standpoint, the advantages of the method are confirmed by real synthesis. The RF-MVDR core uses no DSP48 blocks at all (Section 3.5.1): the decision tree reduces to comparators and Block-RAM look-ups, which frees the scarce hardware multipliers for FFT and channel-coding tasks. The weight-computation latency is about 3.0 μs—4.1× lower than that of the classical MVDR (Section 3.5.2)—enabling adaptation in every frame time slot. The bit-exact co-simulation (Section 3.5.3) confirms the functional equivalence of the synthesized core to the software model, i.e., the move to hardware introduces no inference error beyond the built-in quantization. Together, these results substantiate the readiness of the core for deployment in McWiLL equipment.

At the same time, the proposed approach has limitations. The accuracy of RF-MVDR is bounded both by the approximation resolution (the SINR saturation at high SNR) and by the fundamental self-suppression effect when a null is placed very close to the desired signal—the latter being inherent to the classical MVDR as well. The model quality depends on the coverage of the training set: when the geometry leaves the training distribution (e.g., multipath not represented in training), retraining is required.

5. Conclusions

This work proposed and experimentally validated RF-MVDR, a fast adaptive beamforming algorithm based on a Random Forest, for the McWiLL "Korona" ring antenna arrays. The trained tree ensemble predicts the weight vector directly from the statistics of a single covariance snapshot, replacing the covariance-matrix inversion of the classical MVDR with non-iterative inference. The completeness of the solution was verified end-to-end: MATLAB 2023b simulation, HDL Coder $\rightarrow$ Vivado synthesis for a Kintex-7 device, and bit-exact RTL co-simulation.

The principal advantages of the method are as follows:

- MVDR-class selectivity. The radiation patterns and output SINR of RF-MVDR virtually coincide with classical MVDR across the uplink operating range; the gap does not exceed ≈2 dB for SNR up to ≈20 dB.
- Instantaneous adaptation. The weights are computed from a single snapshot, without iterative convergence, outperforming LMS and RLS in high-mobility scenarios with N = 32 pilots.

- Robustness. Under a low snapshot count, phase errors, and multipath, RF-MVDR retains a high SINR and surpasses the neural-network baseline (MLP) owing to the smoothing effect of ensemble averaging.
- Automatic mutual-coupling handling. Training on data that already contain mutual-coupling effects removes the need for online calibration and multiplication by the inverse coupling matrix.
- Hardware efficiency. The synthesized core uses no DSP48 blocks, has a latency of ≈3.0 μs (4.1× lower than classical MVDR), and is functionally equivalent to the software model as confirmed by bit-exact co-simulation.

Together, these properties make the algorithm suitable for deployment directly in McWiLL equipment and in architecturally similar broadband wireless-access systems with circular arrays operating under high subscriber mobility and dense interference—professional public-safety radio, industrial and transport networks, and prospective receiver chains where a shortage of hardware multipliers requires freeing DSP resources for FFT and channel coding.

Author Contributions: Conceptualization, B.M.K. and D.S.C.; methodology, B.M.K. and D.S.C.; software, B.M.K.; validation, B.M.K. and D.S.C.; formal analysis, B.M.K.; investigation, B.M.K.; resources, D.S.C.; data curation, B.M.K.; writing—original draft preparation, B.M.K.; writing—review and editing, D.S.C.; visualization, B.M.K.; supervision, D.S.C. All authors have read and agreed to the published version of the manuscript.

Funding: This research received no external funding.

Data Availability Statement: The original contributions presented in this study are included in the article. Further inquiries can be directed to the corresponding author.

Acknowledgments: During the preparation of this manuscript, the authors used Perplexity, powered by GPT-5.1, solely for refining the wording of the text. The authors independently prepared the content of the work and take full responsibility for its contents.

Conflicts of Interest: The authors declare no conflicts of interest.

Abbreviations

The following abbreviations are used in this manuscript:

5G	Fifth Generation
AGC	Automatic Gain Control
BRAM	Block Random Access Memory
BTS	Base Transceiver Station
CDMA	Code Division Multiple Access
CS-OFDMA	Code-Spread Orthogonal Frequency Division Multiple Access
DoA	Direction of Arrival
DSP48	Digital Signal Processing slice
FF	Flip-Flop
FPGA	Field-Programmable Gate Array
HDL	Hardware Description Language
INR	Interference-to-Noise Ratio
ITU-R	International Telecommunication Union–Radiocommunication Sector
LMR	Land Mobile Radio
LMS	Least Mean Squares
LTE	Long-Term Evolution
LUT	Look-Up Table
MLP	Multilayer Perceptron
MMSE	Minimum Mean Square Error
MSE	Mean Squared Error

MUSIC	Multiple Signal Classification
MVDR	Minimum Variance Distortionless Response
NLMS	Normalized Least Mean Squares
NR	New Radio
OFDM	Orthogonal Frequency Division Multiplexing
PCA	Principal Component Analysis
PMR	Professional Mobile Radio
RF	Random Forest
RF-MVDR	Random Forest MVDR
RLS	Recursive Least Squares
RMB	Reed-Mallett-Brennan
RTL	Register-Transfer Level
SAS	Smart Antenna System
SCM	Sample Covariance Matrix
SDMA	Spatial Division Multiple Access
SINR	Signal-to-Interference-plus-Noise Ratio
SNR	Signal-to-Noise Ratio
SOI	Signal of Interest
UCA	Uniform Circular Array
ULA	Uniform Linear Array

References

1. Mishra, B.; Singh, A.K.; Satheesha, T.Y.; Verma, R.K.; Singh, V. From past to present: A comprehensive review of antenna technology in modern wireless communication. *J. Eng. Sci. Technol. Rev.* **2024**, *17*, 179–200. [CrossRef]
2. Liu, Y.; Wang, H. Power Normalized and Fractional Power Normalized Least Mean Square Adaptive Beamforming Algorithm. *Electronics* **2026**, *15*, 49. [CrossRef]
3. Mahboob, M.A.; Ashraf, M.A.; Atif, I.; Ikeda, H.; Nwaila, G.T.; Masood, A.; Qureshi, J.; Genc, B.; Khan, I.; Mellado, B. Enhanced Underground Communication: A Circularly Polarized Smart Antenna with Beam Steering for Improved Coverage. *Mining* **2025**, *5*, 14. [CrossRef]
4. Pirapaharan, K.; Ajithkumar, N.; Sarujan, K.; Fernando, X.; Hoole, P.R.P. Smart, Fast, and Low Memory Beam-Steering Antenna Configurations for 5G and Future Wireless Systems. *Electronics* **2022**, *11*, 2658. [CrossRef]
5. Averyanov, R.S.; Bokk, G.O.; Volodina, E.E.; Kudin, A.V.; Lokhvitskii, M.S.; Pantikyan, R.T.; Smirnov, A.V.; Shorin, A.O. *Trunking Wideband Access System MAKVIL*; Shorin, O.A., Ed.; ID Media Publisher: Moscow, Russia, 2021. (In Russian)
6. Beijing Xinwei Communication Technology Co., Ltd. *McWiLL 41.01–V5.0: McWiLL V6 Air Interface Physical Layer Specification*; Version 5.0; Beijing Xinwei Communication Technology Co., Ltd.: Beijing, China, 2013.
7. Mainkar, P.M.; Jagtap, G.N.; Mulay, G.N. Analysis of minimum variance distortionless response and least mean square beamforming algorithm for smart antenna. In Proceedings of the 2016 International Conference on Internet of Things and Applications (IOTA), Pune, India, 22–24 January 2016; pp. 213–216. [CrossRef]
8. Liu, Z.-H.; Su, R.-X.; Zhang, T.-T.; Yu, G.; He, C.-F.; Wu, B. Full laser-based Lamb waves array imaging based on the two-dimensional multiple signal classification algorithm. In Proceedings of the 2020 IEEE Far East NDT New Technology & Application Forum (FENDT), Kunming, China, 23–25 October 2020; pp. 169–173. [CrossRef]
9. Khalmatov, B.M.; Chirov, D.S. Study of smart antenna control algorithms in the McWiLL communication system. *Elektrosvyaz* **2025**, *7*, 47–55. (In Russian)
10. Altakhaineh, A.T.; Alrawashdeh, R.; Zhou, J. Machine Learning-Aided Dual-Function Microfluidic SIW Sensor Antenna for Frost and Wildfire Detection Applications. *Energies* **2024**, *17*, 5208. [CrossRef]
11. Marenco, L.; Hupalo, L.E.; Andrade, N.F.; de Figueiredo, F.A. Machine-learning-aided method for optimizing beam selection and interference suppression. *Sci. Rep.* **2024**, *14*, 20103. [CrossRef]
12. Brilhante, D.d.S.; Manjarres, J.C.; Moreira, R.; de Oliveira Veiga, L.; de Rezende, J.F.; Müller, F.; Klautau, A.; Leonel Mendes, L.; de Figueiredo, F.A.P. A Literature Survey on AI-Aided Beamforming and Beam Management for 5G and 6G Systems. *Sensors* **2023**, *23*, 4359. [CrossRef]
13. Li, G.; Liang, S.; Nie, S.; Liu, W.; Yang, Z. Deep neural network-based generalized sidelobe canceller for dual-channel far-field speech recognition. *Neural Netw.* **2021**, *141*, 225–237. [CrossRef]
14. Breiman, L. Random Forests. *Mach. Learn.* **2001**, *45*, 5–32. [CrossRef]

15. Glushankov, E.I.; Korovin, K.O.; Boyko, I.A.; Borisov, M.G. Current state and prospects for the development of adaptive antenna arrays in radio engineering systems. *Vestn. SPbGUT* **2024**, *2*, 1. (In Russian)
16. *ITU-R M.1801-2*; Radio Interface Standards on Broadband Wireless Access Systems, Including Mobile and Nomadic Applications, in the Mobile Service Operating Below 6 GHz. International Telecommunication Union: Geneva, Switzerland, 2013.
17. Liberovskii, N.Y.; Priputin, V.S.; Chirov, D.S. Review of studies on adaptive beamforming and digital signal processing. *Sovrem. Probl. Distantsionnogo Zondirovaniya Zemli Kosmosa* **2021**, *13*, 16–21. (In Russian) [CrossRef]
18. Kozlov, S.V.; Radionovich, V.V. Digital Beamforming Features in Subaperture Antenna Arrays of Highly Informative Space Radars with Aperture Synthesis. *Dokl. BGUIR* **2023**, *21*, 70–74. (In Russian) [CrossRef]
19. Glushankov, E.I.; Tsarik, V.I. Direct adaptation methods for linear and circular antenna arrays in navigation satellite systems. *St. Petersburg Univ. Telecommun.* **2023**, *26*, 6–16. (In Russian)
20. Soldatov, I.V. Overview of methods for improving noise immunity of the satellite radio navigation systems receiving equipment using the adaptive antenna arrays. *Politekhn. Molod. Zh.* **2023**, *5*, 896. (In Russian) [CrossRef]
21. Aung, V.T.; Dmitrenko, A.A. The essence of adaptive suppression of active noise interference. In *Proceedings of the Information Radio Systems and Radiotechnologies-2024, Minsk, Belarus, 21–22 November 2024*; Belarusian State University of Informatics and Radioelectronics: Minsk, Belarus, 2024; pp. 267–270. (In Russian)
22. Bosco, E.; Spairani, E.; Toffali, E.; Meacci, V.; Ramalli, A.; Matrone, G. A Deep Learning Approach for Beamforming and Contrast Enhancement of Ultrasound Images in Monostatic Synthetic Aperture Imaging: A Proof-of-Concept. *IEEE Open J. Eng. Med. Biol.* **2024**, *5*, 376–382. [CrossRef]